



Liquid Film Condensation behind Shock Waves on the Cold Wall of a Diaphragmless Vertical Shock Tube: An Experimental Study

H. D. Zhu[†], X. Chen, M. Y. Zhang, K. D. Yang, P. Liu, M. Wu, C. Ding and D. J. Liu

College of Mechanical and Electrical Engineering, Guilin University of Electronic Technology, Guilin, Guangxi 541004, China

[†]Corresponding Author Email: zhuhaidong@guet.edu.cn

(Received April 21, 2021; accepted February 19, 2022)

ABSTRACT

The aim of this study was to investigate the condensation of HFC-134a vapor on a shock tube wall behind shock waves. The time-dependent thickness of the condensed liquid film was measured using an optical interference method based on multiple reflections of a laser beam. The condensation on the wall was accompanied by an instantaneous increase in the pressure behind the incident shock wave, and when the reflected shock wave reached the observation window, condensation occurred again. In this experimental study, the characteristics of the diaphragmless vertical shock tube were verified. Reliable experimental data could be obtained using the shock tube. The shock waves could be visualized to study their behaviors in different time periods. The experimental results confirmed the formation of a liquid film on the cold wall of the shock tube after the passing of incident and reflected shock waves, with the liquid film behind the incident shock wave exhibiting a faster formation.

Keywords: Diaphragmless shock tube; HFC-134a vapor; Liquid film; Optical interference method; Shock waves.

NOMENCLATURE

a speed of sound
 I energy reflectivity
 K output voltage from the photodiode
 Q relative energy reflectivity
 L latent heat
 r reflectivity
 V output voltage from the bridge circuit
 γ heat capacity ratio
 δ growth of liquid film
 θ incident angle of laser beam
 η temperature coefficient of resistance
 κ thermal conductivity

Subscripts:

bl boundary layer
i incident shock wave
l liquid film
r reflected shock
s glass
st stagnant
v vapor
1 initial state of the driven gas
2 area behind the incident shock wave
4 initial state of the driver gas
5 area behind the reflected shock wave

1. INTRODUCTION

Interference of shock waves and condensation are observed in various engineering fields (Myers and Hammond 1999). For example, the condensation phenomenon is observed around an aircraft passing through rain clouds and in the internal flows of high-speed pumps or vapor turbines (Honsek and Habashi 2006). Particularly in the low-temperature region, as the speed of sound in vapor is lower than that at

ambient temperature, the interference of the shock waves and two-phase flow easily occurs (Myers *et al.* 2002). Further intensification of this interference can lead to phenomena, such as erosion or vibration, with the worst case being equipment or pipeline damage. To prevent these issues, it is important to clarify the impact of condensation that occurs behind shock waves (Fujikawa *et al.* 1987). Stodola (1927) was the first researcher to study the phenomenon of shock wave condensation. He conducted an experiment on supersaturated steam vapor-liquid

two-phase flow inside a steam turbine in the 1920s. Goldstein (1964) studied the condensation of water vapor on shock tube walls and calculated the condensation coefficient of water vapor. Optical interference techniques have been used in the measurement of the condensed liquid film formed on the end of a tube behind the reflected shock wave (Fujikawa *et al.* 2011; Kanagawa *et al.* 2010; Kobayashi *et al.* 2016; Maerefat *et al.* 1989; Matsumoto and Fujikawa 1997). The condensation coefficients of methanol, ethanol, and carbon tetrachloride vapor were determined (Yano *et al.* 2005; Maerefat *et al.* 1990; Kobayashi *et al.* 2008). Jiang *et al.* (2016) studied the flow characteristics and condensation mechanism of methane steam nonane mixture in supersonic flow. They found that when spontaneous condensation occurs, the pressure, temperature, and Mach number change abruptly due to the release of latent heat. Pillai *et al.* (2018) reported a sudden change in the density and a decrease in the shear stress of the condensation wall in the vicinity of condensation behind the shock wave, causing a rapid drop in the friction of the condensation wall. Under a constant inlet pressure, the liquid film thickness varies with the surface roughness of the condensation wall. Bian *et al.* (2019; 2020) studied the liquefaction process of a methane binary mixture in a supersonic nozzle, the condensation characteristics of different components of natural gas, and the influences of inlet pressure and temperature on the supersonic condensation process. Cao *et al.* (2019; 2021) clarified the position of shock waves in a Laval nozzle, compared the flow field characteristics of condensation and isentropic flows, and studied the low-temperature liquefaction characteristics of methane gas in the Laval nozzle. A shock tube, which a device for generating shock waves, has supported experimental studies. In recent years, some novel shock tubes have been designed. Haylett *et al.* (2012) developed an aerosol shock tube to study the chemical kinetics of low-vapor pressure fuels. These improvements have helped extend the fuel concentration range and improve the spatial uniformity. Long *et al.* (2014) designed and

processed a set of vertical annular coaxial diaphragmless shock tubes, which improved the formation of the fluid interface and helped observe the flow field. Mejia-Alvarez *et al.* (2015) designed a new two-piece driver to replace the traditional diaphragm shock tube. It could reduce the experimental time and make the shock wave more pure. Li *et al.* (2019) designed a circular cross-section open shock tube driven by the high-pressure explosive gas generated by the detonation transmission tube. It was used to perform pressure measurements and flow visualization in the driven tube to study the shock tube performance. However, few have studied shock wave phenomena at low temperatures and condensation phenomenon at the tube end behind the incident and reflected shock waves.

In this experimental study, a diaphragmless vertical shock tube was used to generate shock waves, and a laser interference system helped measure the condensate film thickness. HFC-134a vapor was used as the driven gas in a low-temperature environment. The condensation phenomenon on the low-temperature sidewall surface behind the shock wave was studied.

2. EXPERIMENTAL DEVICE

2.1 Structure of a diaphragmless vertical shock tube

In this study, experiments were carried out using a diaphragmless vertical cryogenic shock tube as shown in Fig. 1. The diaphragm is replaced by two pistons in a high-pressure chamber (Zhang *et al.* 2020). The conventional shock tube has a simple structure; however, it produces broken fragments that disturb the flow field in the shock rupture process. The flange connection of the low-pressure part of the diaphragm shock tube will be opened so that the diaphragm can be replaced after each experiment. At this time, the water vapor in the air flows into the low-pressure part. If the water vapor

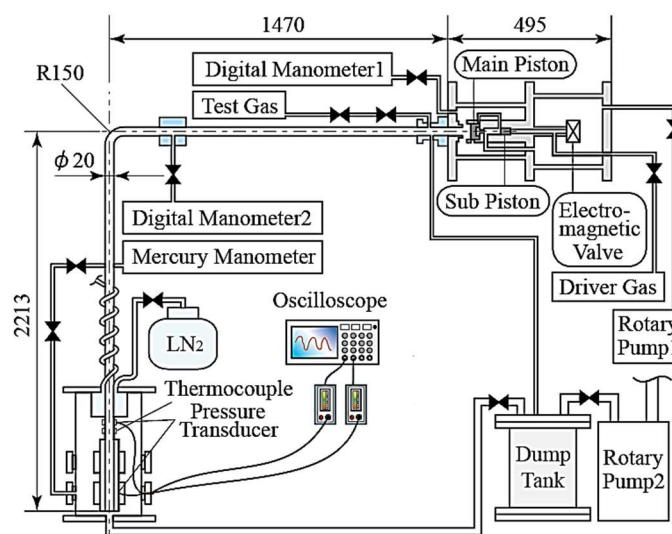


Fig. 1. Diaphragmless vertical shock tube.

condenses on the pipe wall of the observation section, it will cause significant errors in the subsequent experiments. Therefore, in low-temperature experiments, the use of diaphragm shock tubes is associated with a lower efficiency; the process will take approximately 1.5 h. However, a diaphragmless shock tube can be used for continuous experiments without water vapor because there is no diaphragm to be replaced. In this work, to create a low-temperature condition, the cooling equipment and adiabatic equipment in the low-pressure tube were adjusted, and liquid nitrogen was poured into a cooling chamber set above. The test section was covered in a vacuum shield chamber. The pressures of the incident and reflected shock waves were monitored using two piezoelectric transducers installed in the test section. The initial temperature was measured using a temperature sensor. Regarding the operating method of the shock tube, the required shock Mach number should be determined first. Subsequently, the predetermined pressure required for the high-pressure chamber and the low-pressure section is determined. When the shock tube is working, first, the high-pressure chamber is pressurized. At this time, the solenoid valve port is closed, and the valve connected to the waste cylinder is closed. When the driving gas enters the inner cavity of the high-pressure chamber, the main piston and auxiliary piston will both move to the left due to the gas pressure. The pressure gauge 1 is monitored. When the predetermined pressure is reached, the vacuum pump 1 is switched off.

The driven gas is then introduced, and when the predetermined pressure is reached, the valve connected to the driven gas cylinder is closed. When the target cooling temperature is reached, the solenoid valve is opened. Due to the gas pressure, both the main piston and the auxiliary piston move quickly to the right. At this time, the high-pressure chamber and the low-pressure section are connected, and the gas in the high-pressure cylinder rushes into the low-pressure section. Shock waves are generated in the low-pressure section. As they reach the observation section, the shock waves are observed, measured, and studied.

2.2 Characteristic verification of diaphragmless vertical shock tube

Given the use of a new type of shock tube, we applied the Rankine–Hugoniot equations to verify its characteristics to confirm the reliability of the experimental data in this experimental study. Rankine–Hugoniot equations are thermodynamical equations derived from the laws of conservation of mass, momentum, and energy. It relates the velocity of a shock wave to the pressure, density, and temperature of the transmitting fluid before and after the shock wave passes (Krehl 2015).

We applied the ideal, one-dimensional shock wave theory to the shock tube. The following assumptions were made in the present analysis:

1. The mixture flow is one-dimensional.

2. The vapor and gas are thermally perfect, with internal degrees of freedom; and the thermodynamic relationship between the gas molecules is ignored.

3. The dissipative effects of viscosity and thermal conductivity are neglected.

4. Membrane is opened momentarily, and then, a shock wave dependent on the initial condition is formed.

It is more convenient to calculate the change in the parameters of the normal shock wave if we express the parameters with M_i and M_r . To use the Rankine–Hugoniot equation in the calculation of this experiment more conveniently, the equation is transformed as follows:

$$\frac{p_2}{p_1} = \frac{2\gamma_1 M_i^2 - (\gamma_1 - 1)}{\gamma_1 + 1} \tag{1}$$

$$\frac{p_4}{p_1} = \frac{2\gamma_1 M_i^2 - (\gamma_1 - 1)}{\gamma_1 + 1} \left[1 - \frac{\gamma_4 - 1}{\gamma_1 + 1} \frac{a_1}{a_4} \left(M_i - \frac{1}{M_i} \right) \right]^{\frac{-2\gamma_4}{\gamma_4 - 1}} \tag{2}$$

$$\frac{p_5}{p_2} = \frac{(3\gamma_1 - 1)M_i^2 - (\gamma_1 - 1)}{(\gamma_1 - 1)M_i^2 + 2} \tag{3}$$

$$M_r = \left[\frac{2\gamma_1 M_i^2 - (\gamma_1 - 1)}{(\gamma_1 - 1)M_i^2 + 2} \right]^{\frac{1}{2}} \tag{4}$$

The results obtained using the above four equations are used as theoretical values to verify the characteristics of the shock tube for a comparison with the experimental values.

Figure 2 compares the experimental points and theoretical curves of p_{41} and M_i in two different temperature regions. p_{41} is the ratio of the driving gas pressure to the driven gas pressure. Clearly, the lower the temperature, the greater the value of M_i when p_{41} is the same. This is related to the decrease in the sound velocity of the gas with temperature. From the three temperature ranges shown in the figure, it can be concluded that the experimental value is consistent with the theoretical value qualitatively; however, the measured value of M_i is slightly lower than the theoretical value quantitatively. The measured value is approximately

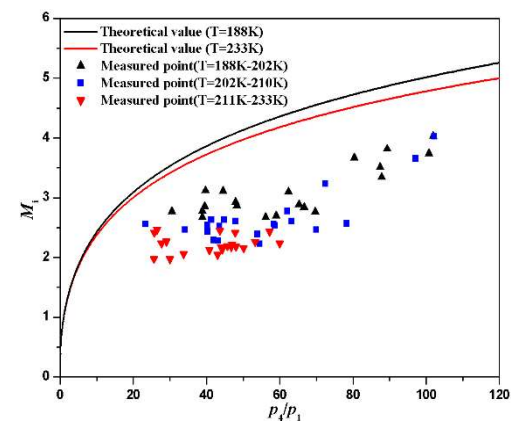


Fig. 2. Relationship between p_{41} and M_i .

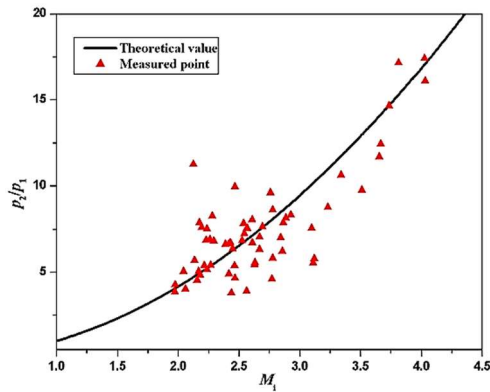


Fig. 3. Relationship between M_i and p_{21} .

70% of the theoretical value. Due to the structure of the shock tube, the shock wave generated by the finite speed and high-speed drive of the piston does not form instantaneously and propagate at a constant propagation speed as in the simple theory; it is generated corresponding to the continuous movement of the two pistons. In the process of shock wave generation, the time required for piston movement is lower than that required in the diaphragm shock tube. The shock wave is slower than the shock wave produced by the diaphragm shock tube under the same conditions. To generate shock waves, the time required for the two pistons to move ranges from 0.3 ms to 0.7 ms. Nevertheless, as shown in Fig. 11(b) and Fig. 11(c) at times t_2 and t_2' , the shock wave visualization image shows that the shock wave is indeed a plane shock wave.

Figure 3 compares the experimental points and theoretical curves of M_i and p_{21} . p_{21} is the ratio of the pressure in the area behind the incident shock wave to the pressure of the driven gas. As shown, the measured point generally conforms to the growth law that p_{21} increases with the increase in M_i . The experimental points are distributed on both sides of the theoretical curve but there remain certain errors. The reason for the errors is that a certain vibration occurs during the operation of the shock tube, particularly after the condensing system is installed. Since the condensing system contacts the ground, the vibration of the low-pressure portion would be more intense, resulting in an unstable p_2 value. Therefore, there is an uncontrollable error between the experimental point and the theoretical curve.

Figure 4 compares the experimental points and theoretical curves of M_i and p_{52} . p_{52} is the ratio of the pressure in the area behind the reflected shock wave to the area behind the incident shock wave. The values of the measured points are slightly scattered, because the flow field behind the reflected shock wave is too complicated, which leads to a large error in the value of p_5 . Nevertheless, as shown in Fig. 11(d) at time t_3 , the reflected shock wave does exist, and the phenomenon is evident. The trends in the measured point and the theoretical curve are also the same.

Figure 5 compares the experimental points and theoretical curves of M_i and M_r . The reflected shock

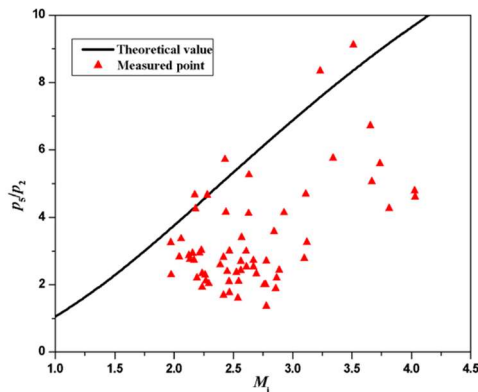


Fig. 4. Relationship between M_i and p_{52} .

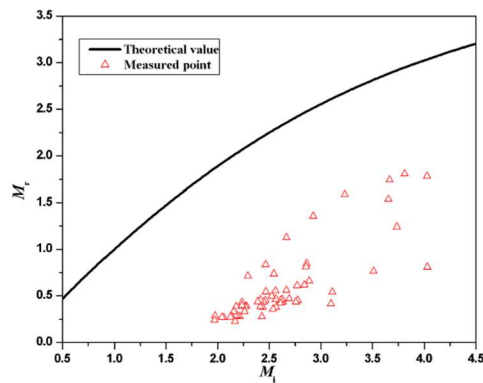


Fig. 5. Relationship between M_i and M_r .

wave is disturbed by the boundary layer formed behind the incident shock wave. The reflected shock wave Mach number after being disturbed decreases. The boundary layer is introduced in the next chapter.

3. RESEARCH METHOD

3.1 Properties of the experimental vapor

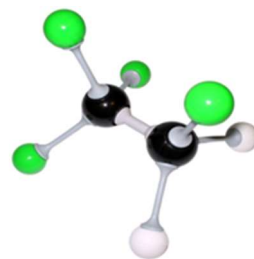


Fig. 6. Schematic of the chemical formula of HFC-134a

Table 1 Parameters of the driven vapor

Chemical formula	CH ₂ F-CF ₃
Molecular weight	102.031
Boiling point	246.97 K (at 101.325 kPa)
Freezing point	172 K (at 101.325 kPa)
Latent heat of liquefaction	177.99 kJ/kg
Specific heat ratio (steam)	1.1186 (at 298.15 K, 101.325 kPa)

3.2 Method of liquid film measurement

The vapor undergoes a phase change to become a liquid and condenses if the gas continues to be pressurized or comes in contact with a cooling surface whose temperature is lower than the saturation temperature when the steam pressure exceeds its saturation pressure. Its form can be divided into liquid film condensation and droplet condensation. When pure vapor condenses on a clean surface, its condensate will form a continuous film on the cold wall; this process is called liquid film condensation. In liquid film condensation, the effect of surface tension is negligible in most cases, so it is easy to analyze. In this experimental study, an ideal film condensation is considered. The saturation of the vapor is necessary for this experiment. When the incident shock wave passes through the shock tube, the pressure gradually increases. Theoretically, the saturated vapor pressure increases following a quadratic curve with the increase in the temperature, and steam condensation will not easily occur. The temperature rise of the steam near the cold wall of the shock tube is suppressed when the pressure suddenly increases, and the steam becomes supersaturated. Therefore, the vapor condenses near the cold wall behind the shock wave. The condensed vapor becomes a liquid film and adheres to the wall surface. Its thickness will increase over time. This is the condensation process of steam on the cold wall behind the shock wave. The liquid film is extremely thin, approximately hundreds of nanometers and is believed to develop in the boundary layer. Typically, the growth of the liquid film ends when it reaches the contact surface. Figure 7 shows the state of the boundary layer and liquid film behind the incident shock wave.

Figure 8 shows the optical interference system along with its layout used for capturing images in this experimental study. In the optical interference system, a He-Ne laser beam is injected through an external observation window. The laser beam is reflected and refracted, and then enters the internal observation window. A part of the laser beam enters the liquid film while the rest is reflected on the liquid film side of the inner observation window. The information received by the photodiode is in the form of interference between the light reflected on this surface and the light that has passed through the liquid film. The captured measurement signal is stored in a computer through the oscilloscope. The experiment with the optical interference system and the shock wave visualization experiment were performed simultaneously.

3.3 Method of calculating related physical quantities

The liquid film formed on the surface of the glass sidewall behind the incident and reflected shock waves grows over time. The laser beam is partially transmitted and partially reflected through the interface between the window and the liquid film. Because of the liquid film growth, the optical system produces an interference pattern, and the energy reflectivity of the laser-reflected light changes. The photodiode detects the light intensity. Based on the

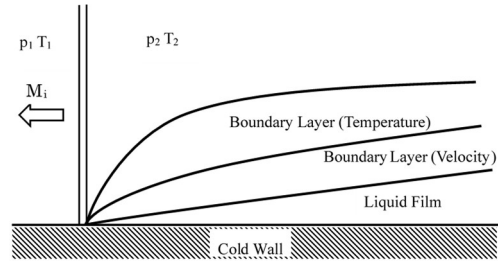


Fig. 7. Boundary layer and liquid film behind an incident shock wave (Brown and Williams 1975; Lighthill 1953).

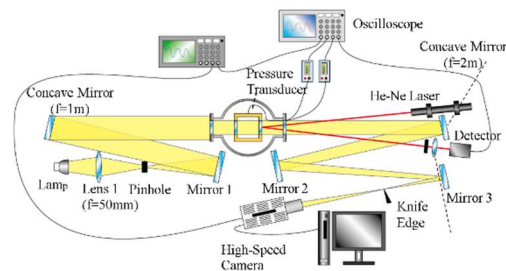


Fig. 8. Layout of the optical interference system and shock wave visualization system.

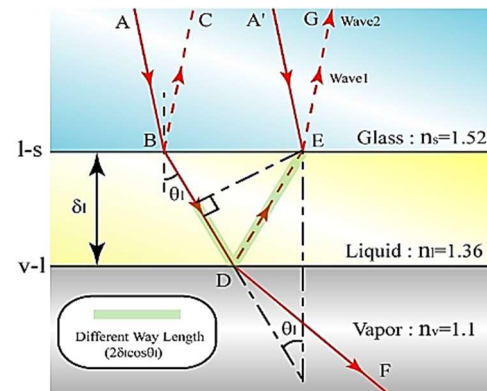


Fig. 9. Principle of the laser interference measurement.

change in the light intensity, the change in the liquid film thickness with time can be determined (Hsu *et al.* 2005). Figure 9 shows the laser interference measurement method. The refractive indices of the observation glass, test gas liquid film, and test gas vapor are denoted by n_s , n_l , and n_v , respectively. HFC-134a was used as the experimental gas in this study, where $n_s = 1.52$, $n_l = 1.30$, and $n_v = 1.1$.

As shown in Fig. 9, Wave1 and Wave2 propagating at the same wavelength and in the same direction interfere with each other. The liquid film thickness measurement based on the interference light is divided into two parts. The first part is the method of calculating the liquid film thickness at the fringe part where the interference signal reaches the peak and intensifies into light waves with large amplitude. When the phase is shifted by half a wavelength π , the

light waves interfere and attenuate into light waves with a small amplitude. In the model studied, the condition for constructing the enhanced interference light is as follows:

$$2\delta_l \cos \theta_l = m\lambda_l \quad (5)$$

where $2\delta_l \cos \theta_l$ represents the different way length. The refractive index (n_l) of the liquid film is used to express the above equation. When the reflected light is enhanced, the liquid film thickness can be expressed as follows:

$$\delta_l = m\lambda_l / (2n_l \cos \theta_l) \quad (6)$$

In the second stage, the liquid film thickness is measured based on the change in the intensity of the reflected light. The liquid film thickness was calculated using this method by comparing with the method of measuring the liquid film thickness of the fringe part of the first section. The reflectance at the interface between the test gas liquid film and the observation glass can be expressed as follows:

$$r_{ls} = \frac{n_l \cos \theta_l - n_s \cos \theta_s}{n_l \cos \theta_l + n_s \cos \theta_s} \quad (7)$$

Similarly, the reflectivity at the interface between the test gas vapor and the test gas liquid film is expressed as

$$r_{vl} = \frac{n_v \cos \theta_v - n_l \cos \theta_l}{n_v \cos \theta_v + n_l \cos \theta_l} \quad (8)$$

When a wavelength leaves a certain point, the phase will be delayed by 2π in the periodically changing waveform. The value of the phase lag is calculated by (9).

$$\varphi_l = 4\pi n_l \delta_l \cos \theta_l / \lambda \quad (9)$$

Since the amplitude of the reflected light from the film is the overlap of these multiple reflected lights, it is necessary to include the sum of all the amplitudes when calculating the energy reflectivity.

$$I(t) = \frac{r_{ls}^2 + r_{vl}^2 + 2r_{ls}r_{vl} \cos \varphi_l}{1 + r_{ls}^2 r_{vl}^2 + 2r_{ls}r_{vl} \cos \varphi_l} \quad (10)$$

In addition, if the voltage output of the photodiode actually measured in the experiment is $K(t)$, and it is measured in an area proportional to $I(t)$, the relative energy reflectivity $Q(t)$ can be derived.

$$Q(t) = \frac{I(t) - I_{\min}}{I_{\max} - I_{\min}} = \frac{K(t) - K_{\min}}{K_{\max} - K_{\min}} \quad (11)$$

According to the above information, the formula for the change in the liquid film thickness with time is as follows:

$$\Delta \delta_l(t) = \frac{\lambda}{4\pi n_l \cos \theta_l} \cos^{-1} \left[\frac{c_1 \{I_{\min} + \Delta I \cdot Q(t)\} - c_2}{c_3 \{1 - I_{\min} - \Delta I \cdot Q(t)\}} \right] - \delta_l^0 \quad (12)$$

δ_l^0 is a constant because the phase shift occurs when the initial output of the model is applied. The coefficients c_1 , c_2 , c_3 , and ΔI are respectively expressed as follows:

$$c_1 = 1 + r_{vl}^2 r_{ls}^2 \quad (13)$$

$$c_2 = r_{vl}^2 + r_{ls}^2 \quad (14)$$

$$c_3 = 2r_{vl}r_{ls} \quad (15)$$

$$\Delta I = I_{\max} - I_{\min} \quad (16)$$

Since the increase in the liquid film can be calculated using Eq. (1), the increase in the liquid film per unit time can be obtained. The condensed mass flux is expressed as follows.

$$m(t) = \rho_l \frac{d\delta_l}{dt} \quad (17)$$

Since the unit of this parameter is $\text{kg}/(\text{m}^2 \cdot \text{s})$, its meaning is the mass of condensation per unit time and per unit area.

Next, the heat flux of the film will be described. When steam condenses, latent heat is released. The heat transfer at this time is considered the heat flux of condensation, expressed as:

$$q_t = m \cdot L = \rho_l L \frac{d\delta_l}{dt} \quad (18)$$

The unit of this parameter is $\text{J}/(\text{m}^2 \cdot \text{s})$ or W/m^2 . Therefore, the heat flux of condensation can also be obtained sequentially over time. When calculating the temperature rise of the stove surface described in the next chapter, the heat flux derived here is used as the boundary condition.

The following two assumptions need to be made:

1. The heat only flows one-dimensionally in the direction perpendicular to the shock tube because the heat flow in the direction parallel to the shock tube of the liquid film is much lower than the heat flow in the direction perpendicular to the shock tube.
2. Glass is considered a semi-infinite solid relative to the direction of heat flow. This is because the heat flow will not penetrate the glass within the time frame of this experiment.

Therefore, the model can be considered a one-dimensional heat conduction problem on a semi-infinite solid. The change in the temperature of the inner wall surface can be approximated as a change in the temperature of the liquid film. The basic equation of this model can be expressed as follows:

$$\frac{\partial T(x,t)}{\partial t} = \frac{\kappa}{\rho \gamma} \frac{\partial^2 T(x,t)}{\partial x^2} \quad (19)$$

We set the initial condition as the temperature distribution at $t = 0$, as follows:

$$T(x,0) = T_0 \quad (20)$$

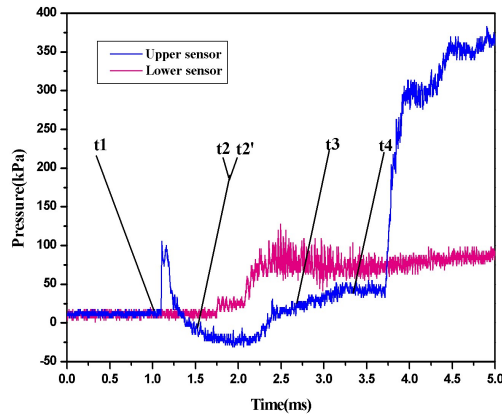


Fig. 10. Pressure readings varying with time obtained from dual sensors.

After the derivation, the temperature from the first point where condensation starts to increase to a specific N th point in step of 10^{-3} ms is expressed as follows:

$$T(N\Delta t) = \frac{2\sqrt{\alpha}}{\kappa\sqrt{\pi}} \left[\sum_{n=1}^N q_n (\sqrt{n\Delta t} - \sqrt{(n-1)\Delta t}) \right] \quad (21)$$

4. EXPERIMENTAL RESULTS AND DISCUSSION

4.1 Visualization of shock waves

When the shock wave passes through the observation section of the shock tube, the signals from the two pressure sensors rise. The readings of the upper sensor and the signal of the lower sensor are both inputted to the oscilloscope. When the rising signal of the upper sensor is inputted to the oscilloscope, the oscilloscope transmits a signal to trigger the high-speed camera. The shooting can last for 2 s, which is sufficient to capture all the phenomena of shock wave incidence and reflection. Figure 10 shows the behavior of the incident and reflected shock waves at each stage. From the pressure waveform, because the incident stimulus passes through the upstream pressure element, the output pressure rises first at 1.096 ms, and the output pressure of the downstream pressure element rises at 1.744 ms. p_2 is obtained

from the rise of the upstream pressure element, and M_i is obtained from the time difference between the rise of the two pressure elements. Subsequently, the incident shock wave is reflected at the end of the shock tube and forms a reflected shock wave. The reflected shock wave passes through the position of the downstream pressure element at 2.122 ms and passes through the position of the upstream pressure element at 3.708 ms. p_5 can be obtained from the downstream pressure sensor, and M_r is obtained from the rise time difference in the two pressure elements. When the time reaches t_3 , a bifurcation due to the reflected shock wave is observed. The reflected shock wave interferes with the boundary layer formed behind the incident shock wave. As shown in Fig. 11, the images of the shock waves can be seen through the visualization system. The shock wave behaviors can be observed in the images at the above time points.

The interference between the reflected shock wave and the boundary layer can be represented using the flow model proposed by Mark (1958), as shown in Fig. 12. The incident shock wave propagates in the shock tube with one end closed, and after being reflected by the closed end wall, a reflected shock wave is generated, and the fluid after the wave is continuously compressed, while interacting with the boundary layer. This is a rapid evolution process over time and space. The reflected shock wave has an evident λ -shaped bifurcated shock wave structure. A curved slip line extends backward from the three-wave point, and there is a significant flow separation zone immediately following the leading bifurcated shock wave under the bifurcated shock wave. Starting from the position close to the front boundary layer, the circulation area of the recirculation zone gradually increases. With the continuous leftward movement of the bifurcated shock wave structure, the vortex structure of different sizes in the recirculation zone also undergoes drastic changes. At the same time, the vortex structure of the tail recirculation zone intersects with the bifurcated tail shock wave, which makes the wave system structure of the entire flow field more complicated. Time t_3 is when the shock wave bifurcation phenomenon occurs, as shown in Fig. 12. From the perspective of the observer, if the coordinates of the reflected shock wave are fixed, the coordinates move at the same

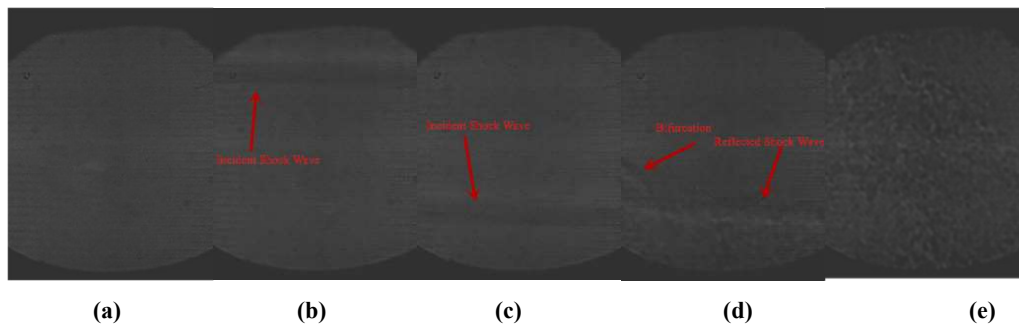


Fig. 11. Behavior of the incident waves and reflected waves: (a) 1.102 ms (t_1), (b) 1492 ms (t_2), (c) 1494 ms (t_2'), (d) 2.731 ms (t_3), and (e) 3.376 ms (t_4).

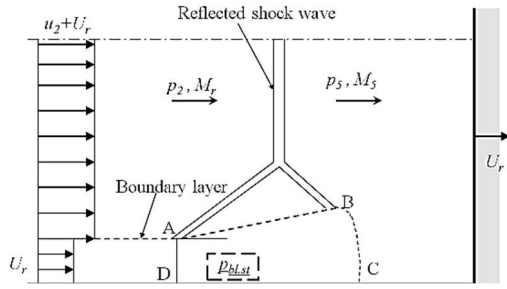


Fig. 12. Interference model between reflected shock wave and boundary layer (Zhou *et al.* 2018).

speed as the reflected shock wave, with U_r as the speed, $U_2 + U_r$ as the flow velocity in the hot air flow region, and U_r as the velocity of the wall surface. The direction of the speed is to the right. Therefore, the Mach number M_{bl} of the boundary layer flow is as follows:

$$M_{bl} = \frac{2(\gamma_1 - 1)M_i^2 + (3 - \gamma_1)}{(\gamma_1 + 1)M_i^2} \quad (22)$$

If the stagnation point pressure of the boundary layer flow is $p_{bl,st}$, when $M_{bl} < 1$, the equation can be expressed as follows:

$$\frac{p_{bl,st}}{p_2} = \left(1 + \frac{\gamma_1 - 1}{2} M_{bl}^2\right)^{\frac{\gamma_1}{\gamma_1 - 1}} \quad (23)$$

When $M_{bl} > 1$, it is assumed that the vertical shock wave decelerates to a subsonic speed. The equation is:

$$\frac{p_{bl,st}}{p_2} = \left(\frac{\gamma_1 - 1}{2} M_{bl}^2\right)^{\frac{\gamma_1}{\gamma_1 - 1}} \left[\frac{\gamma_1 + 1}{2\gamma_1 M_{bl}^2 - (\gamma_1 - 1)}\right]^{\frac{\gamma_1}{\gamma_1 - 1}} \quad (24)$$

If $p_{bl,st}$ is greater than p_5 , the boundary layer flow can move away behind the reflected shock wave, and in this case, the interference between the reflected shock wave and the boundary layer is weak. However, if $p_{bl,st}$ is less than p_5 , the boundary layer flow cannot pass the reflected shock wave. In this case, the boundary layer flow is considered to be confined to the ABCDA region of the bifurcated shock wave foot, as shown in Fig. 10. After the calculation, based on the existing experimental conditions, $M_{bl} < 1$ and $p_{bl,st} < p_5$. Therefore, theoretically, the shock wave bifurcation phenomenon will occur in this experiment.

4.2 Measurements of condensed liquid film growth

Taking a set of experiments as an example, the data obtained from the light receiving device using the laser interference system in this experiment are shown in Fig. 11. The initial conditions of the experiment are marked in the lower left corner of the figure. These data were denoised by Fourier transform. The time required for the incident and reflected shock waves to pass through the observation window can be calculated from the sensor, as shown in Fig. 13. The two dashed lines are marked as the corresponding time behind the

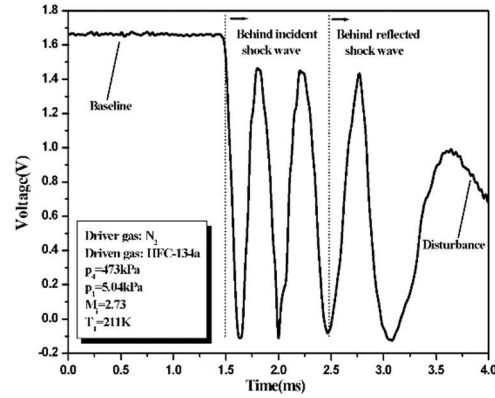


Fig. 13. Interference signal generated by the optical system.

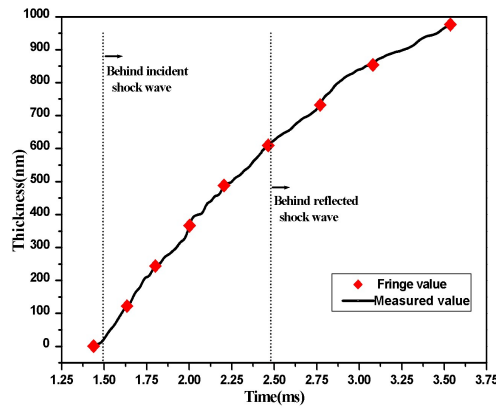


Fig. 14. Liquid film thickness growth curve with time.

incident shock wave and the reflected shock wave in the following figures. When the shock wave passes, this signal can correspond to the calculated value of the signal obtained by the sensor. After the incident shock wave passes, a complete single-cycle interference signal can be obtained because of the liquid film growth. After the reflected shock wave passes, a complete two-cycle interference signal can be obtained because of the liquid film growth. This is sufficient to prove that condensation occurs on the wall after the shock wave passes and that a liquid film is produced on the inner wall. There is a disturbance waveform after the complete interference signal, and reports explaining the reasons for the signal disturbance phenomenon in the rear are limited. We infer that this phenomenon may be due to the complex flow field behind the reflected shock wave that causes a significant number of small fluctuations on the liquid film surface. This disturbs the interference signal. After a period of time following the passage of the reflected shock wave, this phenomenon will become more serious.

We can calculate the liquid film thickness through the interference signal using Eq. (12). The two steps for measuring the liquid film thickness are included in Fig. 14. Each red dot represents a fringe value, which is the ideal liquid film thickness under a monotonous increase. The condensate film growth

calculated by the interference signal from which noise has been removed by the Fourier transform and the growth of the condensate film calculated while increasing monotonously show a high consistency. Clearly, the growth tendency of the liquid film after the incident shock wave is faster than the growth tendency of the liquid film after the reflection shock wave. The shock wave bifurcation phenomenon behind the reflected shock wave may be the cause of the slower growth of the liquid film thickness. The bifurcation affects the boundary layer flow and limits liquid film growth.

The change in the heat flux is the intermediate value of the derivation process between the change in the liquid film thickness and the change in the liquid film temperature. Its value can be derived using Eq. (18). Figure 15 shows the increase in the heat flux with time. The shock tube vibrates when it is working, so the small vibration will be amplified when calculating the heat flux. The red dot in the figure is the average value of one vibration period in the actual measurement value. The black dots in the figure represents fringe values. The fringe value decreases monotonously, which is an ideal increase in the heat flux. The results show that the measured values are evenly distributed on both sides of the fringe value, and the trends are consistent

Therefore, it is important to obtain the theoretical temperature change of the inner wall of the shock tube. The wall temperature change can be calculated using Eq. (21). Figure 16 shows the temperature of the inner wall surface with time. The red line in the figure represents the fringe value. The black line in the figure represents the actual measured values. The initial stage of the liquid film formation is just after the incident shock wave passes through the observation area. The figure shows that the temperature rise rate instantly increases at this time. Subsequently, the growth rate gradually slows down. After the reflected shock wave passes, the temperature growth rate is much lower than the initial stage of liquid film formation.

5. CONCLUSIONS AND FUTURE WORK

In this study, we designed a diaphragmless vertical shock tube equipped with a liquid nitrogen cooling system to perform low-temperature shock experiments. Several shock wave experiments were carried out to verify the characteristics of the diaphragmless shock tube with a cryogenic system. The shock wave parameters conformed to the law of the Rankine–Hugoniot equations, thus proving the reliability of this equipment. Through the shock wave visualization system, the behavior of the shock wave could be observed, including the bifurcation phenomenon of the reflected shock wave. A laser interference system with an He–Ne laser was designed. Both the incident and reflected shock waves produced a liquid film on the inner cold wall of the shock tube, and this phenomenon was observed through the proposed system. From the six sets of typical quantitative experimental data presented in Table 2, the growth of the liquid film

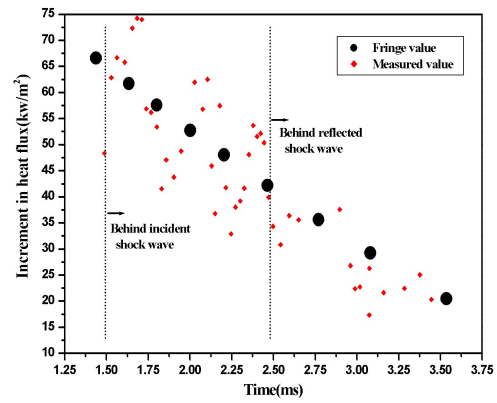


Fig. 15. Change curve of heat flux increment with time

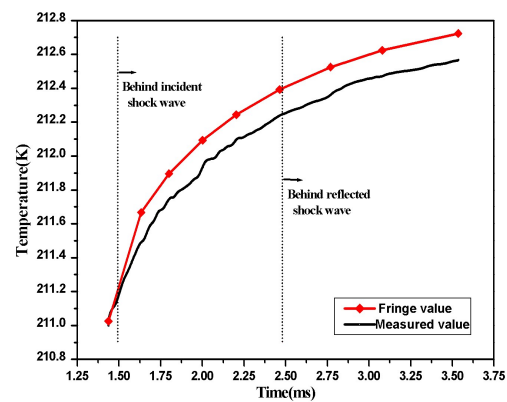


Fig. 16. Theoretical growth curve of the inner wall surface temperature with time

behind the reflected shock waves was found to be slower than the growth of the liquid film behind the incident shock wave. The growth of the liquid film behind the reflected shock waves is denoted by v_{f1} , and the growth of the liquid film behind the incident shock wave is denoted by v_{f2} . This may be due to the shock wave bifurcation phenomenon. In addition, disturbances were detected in the later stages of the generated interference signal, which may be due to the complex flow field behind the reflected shock wave.

Table 2 Growth rate of liquid film under different conditions

p_1 (kPa)	P_4 (kPa)	T_1 (K)	v_{f1} (nm/ms)	v_{f2} (nm/ms)
3.71	401	191	464.15	207.44
4.69	504	191	465.95	188.32
4.59	572	200	664.29	259.66
4.67	490	200	686.97	282.22
5.04	473	211	573.81	330.87
5.77	504	211	484.06	163.06

In a future work, we plan to install a temperature measurement system that fits the inner walls of the shock tube observation part completely. The

temperature data obtained can be compared with the temperature data of the inner wall of the shock tube calculated using the liquid film thickness. Experiments can be performed on the condensation of the liquid film behind the shock wave.

ACKNOWLEDGEMENTS

This work was supported by the Natural Science Foundation of Guangxi Province under Grant number 2017GXNSFAA198122.

REFERENCES

- Bian, J, X. W. Cao, W. Yang, X. D. Song, C. C. Xiang, S. Gao (2019) Condensation characteristics of natural gas in the supersonic liquefaction process. *Energy* 168, 99–110.
- Bian, J, X. W. Cao, W. Yang, D. Guo, C. C. Xiang. (2020) Prediction of supersonic condensation process of methane gas considering real gas effects. *Applied Thermal Engineering* 164: 114508.
- Brown, S. N. and P. G. Williams (1975). Self-induced Separation. III. *IMA. Journal of Applied Mathematics* 16(2), 175-191.
- Cao, X. W., J. Bian (2019) Supersonic separation technology for natural gas processing: A review. *Chemical Engineering and Processing - Process Intensification* 136, 138-151.
- Cao, X. W., Y. Liu, X. R. Zang, D. Guo, J. Bian (2021) Supersonic refrigeration performances of nozzles and phase transition characteristics of wet natural gas considering shock wave effects. *Case Studies in Thermal Engineering* 24, 100833.
- Fujikawa, S., M. Okuda, T. Akamatsu and T. Goto (1987). Non-equilibrium vapour condensation on a shock-tube endwall behind a reflected shock wave. *Journal of Fluid Mechanics* 183, 293-324.
- Fujikawa, S., T. Yano and M. Watanabe (2011). Methods for the Measurement of Evaporation and Condensation Coefficients. In S. Fujikawa (ed.), *Vapor-Liquid Interfaces, Bubbles and Droplets: Fundamentals and Applications*, Berlin, Heidelberg, 71-109, Springer Berlin Heidelberg.
- Goldstein, R. (1964). Study of Water Vapor Condensation on Shock-Tube Walls. *The Journal of Chemical Physics* 40(10), 2793-2799.
- Haylett, D. R., D. F. Davidson and R. K. Hanson (2012). Second-generation aerosol shock tube: an improved design. *Shock Waves* 22(6), 483-493.
- Honsek, R. and W. G. Habashi (2006). FENSAP-ICE: Eulerian Modeling of Droplet Impingement in the SLD Regime of Aircraft Icing. In *44th AIAA Aerospace Sciences Meeting and Exhibit*, American Institute of Aeronautics and Astronautics.
- Hsu, C. C., J. Y. Lee and D. C. Su (2005). Thickness and optical constants measurement of thin film growth with circular heterodyne interferometry. *Thin Solid Films* 491(1),91-95.
- Jiang, W.M., J. Bian, Y. Liu, Z. L. Liu, L. Teng, G. Geng (2016). Investigation of flow characteristics and the condensation mechanism of ternary mixture in a supersonic nozzle. *Journal of Natural Gas Science and Engineering* 34, 1054-1061.
- Kanagawa, T., T. Yano, M. Watanabe and S. Fujikawa (2010). Unified Theory Based on Parameter Scaling for Derivation of Nonlinear Wave Equations in Bubbly Liquids. *Journal of Fluid Science and Technology* 5(3), 351-369.
- Kobayashi, K., K. Konno, H. Yaguchi, H. Fujii, T. Sanada and M. Watanabe (2016). Early stage of nanodroplet impact on solid wall. *Physics of Fluids* 28(3), 032002.
- Kobayashi, K., S. Watanabe, D. Yamano, T. Yano and S. Fujikawa (2008). Condensation coefficient of water in a weak condensation state. *Fluid Dynamics Research* 40(7-8), 585-596.
- Krehl, P. O. K. (2015). The classical Rankine-Hugoniot jump conditions, an important cornerstone of modern shock wave physics: ideal assumptions vs. reality. *The European Physical Journal H* 40(2), 159-204.
- Li, G., T. Ukai and K. Kontis (2019). Characterization of a novel open-ended shock tube facility based on detonation transmission tubing. *Aerospace Science and Technology* 94, 105388.
- Lighthill, M. J. (1953). On Boundary Layers and Upstream Influence. II. Supersonic Flows without Separation. *Proceedings of the Royal Society of London. Series A, Mathematical and Physical Sciences* 217(1131), 478-507.
- Long, T., Z. G. Zhai, T. Si and X. S. Luo (2014). Design and validation of vertical annular shock tube for RM instability study. *Journal of Experiments in Fluid Mechanics* 28(06),86-91.
- Maerefat, M., T. Akamatsu and S. Fujikawa (1990). Non-equilibrium condensation of water and carbontetrachloride vapour in a shock-tube. *Experiments in Fluids* 9(6),345-351.
- Maerefat, M., S. Fujikawa, T. Akamatsu, T. Goto and T. Mizutani (1989). An experimental study of non-equilibrium vapour condensation in a shock-tube. *Experiments in Fluids* 7(8),513-520.
- Mark, H. (1985). *The interaction of a reflected shock wave with the boundary layer in a shock tube*. National Advisory Committee for Aeronautics.
- Matsumoto, M. and S. Fujikawa (1997). Nonequilibrium vapor condensation: molecular simulation and shock-tube experiment. *Microscale Thermophysical Engineering*

- 1(2),119-126.
- Mejia-Alvarez, R., B. Wilson, M. C. Leftwich, A. A. Martinez and K. P. Prestridge (2015). Design of a fast diaphragmless shock tube driver. *Shock Waves* 25(6),635-650.
- Myers, T. G., J. P. F. Charpin and C. P. Thompson (2002). Slowly accreting ice due to supercooled water impacting on a cold surface. *Physics of Fluids* 14(1),240-256.
- Myers, T. G. and D. W. Hammond (1999). Ice and water film growth from incoming supercooled droplets. *International Journal of Heat and Mass Transfer* 42(12),2233-2242.
- Pillai, A. and B. Prasad (2018). Effect of wall surface roughness on condensation shock. *International Journal of Thermal Sciences* 132,435-445.
- Stodola, A. (1927). Steam and Gas Turbines. *Simulation of Industrial Processes for Control Engineers* 3,20-23.
- Yano, T., K. Kobayashi and S. Fujikawa (2005). Condensation of methanol vapor onto its liquid film on a solid wall behind a reflected shock wave. *AIP Conference Proceedings* 762(1), 208-213.
- Zhang, M. Y., X. Chen, P. Liu, K. D. Yang and H. D. Zhu (2020). Design of Diaphragmless Shock Tube and Research on its Normal Temperature Characteristics. *Journal of Physics: Conference Series* 1601,062018.
- Zhou, G., K. Xu and F. Liu (2018). Grid-converged solution and analysis of the unsteady viscous flow in a two-dimensional shock tube. *Physics of Fluids* 30(1),016102.